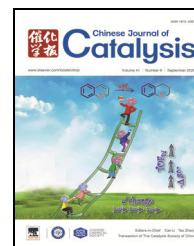


available at [www.sciencedirect.com](http://www.sciencedirect.com)journal homepage: [www.elsevier.com/locate/chnjc](http://www.elsevier.com/locate/chnjc)

## Article

# A reconstruction strategy for the synthesis of Cu-SAPO-34 with excellent NH<sub>3</sub>-SCR catalytic performance and hydrothermal stability

Lijing Sun <sup>a,b</sup>, Miao Yang <sup>a</sup>, Yi Cao <sup>a,c</sup>, Peng Tian <sup>a,\*</sup>, Pengfei Wu <sup>a,b</sup>, Lei Cao <sup>a</sup>, Shutao Xu <sup>a</sup>, Shu Zeng <sup>a,b</sup>, Zhongmin Liu <sup>a,#</sup>

<sup>a</sup> National Engineering Laboratory for Methanol to Olefins, Dalian Institute of Chemical Physics, Chinese Academy of Sciences, Dalian 116023, Liaoning, China

<sup>b</sup> University of Chinese Academy of Sciences, Beijing 100049, China

<sup>c</sup> School of Material Science and Chemical Engineering, Ningbo University, Ningbo 315211, Zhejiang, China



## ARTICLE INFO

## Article history:

Received 16 January 2020

Accepted 27 February 2020

Published 5 September 2020

## Keywords:

Cu-SAPO-34

Hydrothermal synthesis

NH<sub>3</sub>-SCR

Hydrothermal stability

Crystallization

## ABSTRACT

A reconstruction strategy has been developed to synthesize Cu-SAPO-34 with a wide crystallization phase region, high solid yield, and tunable Si and Cu contents. Cu-rich SAPO-34 was prepared from a Cu-amine complex, which acted as a precursor and Cu source for the reconstruction synthesis. The role of the Cu-amine complex as a template was restricted, which allowed easier control over the Cu and Si contents than in the previously reported “one-pot” synthesis method. Characterization of the material revealed that the Si(4Al) coordination environment dominates the synthesized Cu-SAPO-34 catalysts. High-temperature hydrothermal treatment increased the isolated Cu<sup>2+</sup> content slightly, and the acid sites in the low-silica catalyst are more resistant to hydrothermal treatment than those of the existing catalysts. The obtained materials, especially the low-silica Cu-SAPO-34 sample, exhibit excellent catalytic activity and hydrothermal stability for the selective catalytic reduction of NO<sub>x</sub> by NH<sub>3</sub> (NH<sub>3</sub>-SCR). In addition, the influence of the catalyst acidity on the NH<sub>3</sub>-SCR reaction was also investigated and is discussed. The high synthetic efficiency and outstanding catalytic performance make Cu-SAPO-34 synthesized by the reconstruction method a promising catalyst for the NH<sub>3</sub>-SCR process.

© 2020, Dalian Institute of Chemical Physics, Chinese Academy of Sciences.

Published by Elsevier B.V. All rights reserved.

## 1. Introduction

The selective catalytic reduction of NO<sub>x</sub> by urea or ammonia (NH<sub>3</sub>-SCR) is one of the most effective technologies to reduce NO<sub>x</sub> emissions from diesel engine exhausts [1,2]. Furthermore, the development of highly efficient and stable catalysts is crucial to meeting the upcoming strict NO<sub>x</sub> emission standards [3]. Among the developed catalysts for the NH<sub>3</sub>-SCR process, tran-

sition-metal-exchanged zeolites are promising candidates, showing attractive NH<sub>3</sub>-SCR performance [4–6]. In particular, the Cu-CHA zeolites, including Cu-SSZ-13 and Cu-SAPO-34, have received considerable attention because of their outstanding NH<sub>3</sub>-SCR activity over a wide temperature range, as well as their high hydrothermal stability [7–10]. In fact, Cu-SSZ-13 is used commercially by the BASF Corporation [8]. Compared to Cu-SSZ-13, Cu-SAPO-34 has unique characteris-

\* Corresponding author. Tel: +86-411-84379218; Fax: +86-411-84699289; E-mail: [tianpeng@dicp.ac.cn](mailto:tianpeng@dicp.ac.cn)

# Corresponding author. Tel: +86-411-84379998; Fax: +86-411-84379289; E-mail: [liuzm@dicp.ac.cn](mailto:liuzm@dicp.ac.cn)

This work was supported by the National Natural Science Foundation of China (21476228, 21606221, 21676262, 21991091), and the Key Research Program of Frontier Sciences, CAS (QYZDB-SSW-JSCO 40).

DOI: 10.1016/S1872-2067(20)63583-5 | <http://www.sciencedirect.com/science/journal/18722067> | Chin. J. Catal., Vol. 41, No. 9, September 2020

tics: On one hand, Cu-SAPO-34 with a comparable Cu loading exhibits a higher activity at a low temperature range (150–200 °C) [11,12], which is suitable for the start-up period of diesel vehicles. On the other hand, Cu-SAPO-34 is more robust to high-temperature steam [11]. In a typical after-treatment system for diesel engines, the SCR unit is normally used together with a diesel particulate filter (DPF), which requires periodic regeneration. A great deal of heat (> 700 °C) is, thus, transferred to the SCR unit from the DPF [2]. Consequently, excellent hydrothermal stability is highly desirable for the NH<sub>3</sub>-SCR catalyst. Finally and advantageously, the preparation cost of Cu-SAPO-34 is quite low. Moreover, the templates for SAPO-34 synthesis are abundant, which favors the manipulation of the features of SAPO-34 to fit reaction requirements.

One of the main problems facing Cu-SAPO-34 is its Cu-loading process, which generally requires time-consuming post-synthetic NH<sub>4</sub><sup>+</sup> and Cu<sup>2+</sup> ion-exchange processes in aqueous solution. During this process, the irreversible hydrolysis of Si–O(H)–Al bonds occurs, which results in structural damage and acidity and crystallinity loss, as well as the formation of CuO<sub>x</sub> clusters, resulting in catalytic performance degradation [13]. Consequently, considerable efforts have been made to optimize the preparation process. Rare earth ions such as Ce<sup>3+</sup> and La<sup>3+</sup> have been used in the ion exchange process and are effective in mitigating dealumination and the aggregation of copper species [14,15]. **A direct ion-exchange (DIE) method was developed by our group to achieve highly crystalline Cu-exchanged SAPO-34s [16]. In particular, calcination at high temperatures (700 °C) was found to be critical for promoting the dispersion of Cu<sup>2+</sup> ions.** In addition, solid-state ion exchange (SSIE), calcination of SAPO-34/CuO mixtures at high temperatures and “one-pot” synthesis, where Cu-containing chemicals such as CuO and CuSO<sub>4</sub> are added during gel preparation, were developed by Gao et al. [17]. Unfortunately, despite the high-temperature calcination step to optimize the Cu<sup>2+</sup> ion distribution, the NH<sub>3</sub>-SCR catalytic activity remains insufficient because of the presence of CuO clusters.

Mirroring the development of molecular sieve synthesis [18], a “one-pot” synthesis of Cu-SAPO-34 using the copper-tetraethylenepentamine (Cu-TEPA) complex as a template and copper source has been developed [19,20]. This method is convenient and facile. Cu<sup>2+</sup> ions are formed after the removal of the organic part of the Cu-TEPA template, which is promising for practical applications. Unfortunately, the use of Cu-TEPA as a structure directing agent tends to result in Cu-SAPO-34 with high Si contents and abundant Si islands, resulting in inferior catalytic performance and hydrothermal stability. Moreover, it is challenging to optimize the Cu and Si contents and their distributions simultaneously. As a template, the Cu-TEPA complex has very strong directing ability toward the CHA structure. Even when using low doses of Cu-TEPA, which reduces the solid yield, the Cu content of the product cannot be decreased completely because of the preferential entry of copper into the CHA structure [19]. Thus, it would be desirable to find an effective way to control the Cu and Si contents and their distributions in this system. Martinez-Franco et al. improved the synthetic method by introducing various competitive templates

[21]. A triple-template system was reported to maximize the solid yield and enhance the hydrothermal stability. However, activity decay was inevitable when the hydrothermal aging temperature was higher than 750 °C [21]. In addition, there were large Si islands in the products, which indicates that there is further scope for the optimization of the “one-pot” synthesis of Cu-SAPO-34 [22].

In this work, we propose a reconstruction strategy to synthesize Cu-SAPO-34 hydrothermally. In this strategy, Cu-rich SAPO-34 is prepared using Cu-TEPA as a precursor and copper source to assist the crystallization of Cu-SAPO-34. Because the role of Cu-TEPA as a template was restricted by the CHA structure and it is the only source of Cu, the synthesis of Cu-SAPO-34 could be controlled by choosing an appropriate template and adjusting the precursor dosage. Thus, Cu-SAPO-34 samples with similar Cu loadings but different Si contents or similar Si contents but different Cu loadings were synthesized and characterized using various techniques including magic angle spinning (MAS) solid-state <sup>13</sup>C and <sup>29</sup>Si NMR, energy dispersive X-ray spectroscopy (EDX), electron paramagnetic resonance (EPR), in situ diffuse reflectance infrared Fourier transform spectroscopy (DRIFTS), scanning electron microscopy (SEM), X-ray diffractometry (XRD), thermogravimetric and differential thermalgravimetric analysis (TGA and DTA, respectively), X-ray fluorescence (XRF) spectroscopy, N<sub>2</sub> adsorption–desorption, hydrogen temperature-programmed reduction (H<sub>2</sub>-TPR), and ammonia temperature-programmed desorption (NH<sub>3</sub>-TPD). The catalytic performance and hydrothermal stability of the compounds were evaluated based on their NH<sub>3</sub>-SCR activities. The effect of the Si content (acidity) of the Cu-SAPO-34 samples on the catalytic performance was also investigated and is discussed.

## 2. Experimental

### 2.1. Synthesis

Three batches of Cu-SAPO-34 precursors with minor compositional differences (Table 1), denoted Cu-SAPO-34-P<sub>n</sub> (where *n* is the batch number), were prepared using a slightly modified version of the “one-pot” procedure reported in the literature [19]. The compositional modification was realized by changing the dosage of the silica source and template. The synthetic details for Cu-SAPO-34-P<sub>n</sub> (*n* = 1–3) can be found in supporting information. The XRD patterns and typical morphologies of the Cu-SAPO-34-P<sub>n</sub> samples are shown in Figs. S1 and S2, respectively.

Cu-SAPO-34 samples with different Cu contents were further synthesized by using the Cu-SAPO-34-P<sub>n</sub> as the Cu source, part Si/P/Al source, and seeds. The synthetic procedure was similar to that of the Cu-SAPO-34-P<sub>n</sub> samples, except for the omission of the Cu-TEPA template and the addition of Cu-SAPO-34-P<sub>n</sub>. Pseudoboehmite (67 wt%) was first dissolved in distilled water, followed by the addition of phosphoric acid (85 wt%), silica sol (31 wt%), diethylamine (DEA), and Cu-SAPO-34-P<sub>n</sub>. The molar proportions of the reactant gel were 0.9 P<sub>2</sub>O<sub>5</sub>/1.0 Al<sub>2</sub>O<sub>3</sub>/*x*SiO<sub>2</sub>/1.9 DEA/55 H<sub>2</sub>O (*x* = 0.4–0.7). The

**Table 1**  
Synthetic conditions <sup>a</sup> and elemental compositions of the samples.

Sample	Gel			Synthesized material		
	xSiO <sub>2</sub>	Precursor Dosage <sup>b</sup>		Composition <sup>c</sup>	Cu loading <sup>c</sup>	Solid yield <sup>d</sup>
Cu-SAPO-34-P1 <sup>e</sup>	0.6	N/A	N/A	Al <sub>0.505</sub> P <sub>0.355</sub> Si <sub>0.140</sub> O <sub>2</sub>	9.0	89.7
Cu-SAPO-34-P2 <sup>e</sup>	0.5	N/A	N/A	Al <sub>0.512</sub> P <sub>0.354</sub> Si <sub>0.134</sub> O <sub>2</sub>	7.1	93.3
Cu-SAPO-34-P3 <sup>e</sup>	0.6	N/A	N/A	Al <sub>0.487</sub> P <sub>0.352</sub> Si <sub>0.161</sub> O <sub>2</sub>	8.8	88.4
1	0.5	Cu-SAPO-34-P1	17	Al <sub>0.491</sub> P <sub>0.374</sub> Si <sub>0.135</sub> O <sub>2</sub>	1.3	73.7
2	0.5	Cu-SAPO-34-P1	44	Al <sub>0.494</sub> P <sub>0.370</sub> Si <sub>0.136</sub> O <sub>2</sub>	2.8	85.4
3	0.5	Cu-SAPO-34-P1	60	Al <sub>0.496</sub> P <sub>0.371</sub> Si <sub>0.133</sub> O <sub>2</sub>	4.1	77.4
4	0.6	Cu-SAPO-34-P1	44	Al <sub>0.489</sub> P <sub>0.368</sub> Si <sub>0.143</sub> O <sub>2</sub>	2.5	87.4
5	0.7	Cu-SAPO-34-P1	44	Al <sub>0.491</sub> P <sub>0.363</sub> Si <sub>0.146</sub> O <sub>2</sub>	2.8	81.8
LSiCu <sub>1.6</sub>	0.4	Cu-SAPO-34-P2	20	Al <sub>0.493</sub> P <sub>0.380</sub> Si <sub>0.127</sub> O <sub>2</sub>	1.6	72.5
HSiCu <sub>1.7</sub>	0.7	Cu-SAPO-34-P2	26	Al <sub>0.483</sub> P <sub>0.360</sub> Si <sub>0.157</sub> O <sub>2</sub>	1.7	84.1
LSiCu <sub>3.4</sub>	0.4	Cu-SAPO-34-P2	49	Al <sub>0.493</sub> P <sub>0.381</sub> Si <sub>0.126</sub> O <sub>2</sub>	3.4	77.3
HSiCu <sub>3.5</sub>	0.6	Cu-SAPO-34-P3	44	Al <sub>0.481</sub> P <sub>0.347</sub> Si <sub>0.172</sub> O <sub>2</sub>	3.5	85.2

<sup>a</sup>The molar ratio was 0.9 P<sub>2</sub>O<sub>5</sub>/1.0 Al<sub>2</sub>O<sub>3</sub>/xSiO<sub>2</sub>/1.9 DEA/55 H<sub>2</sub>O ( $x = 0.4-0.7$ ); all samples were crystallized at 200 °C for 24 h. <sup>b</sup>Precursor dosage =  $W_{\text{Cu-SAPO-34-P}n} \times 85\% / (W_{\text{SiO}_2+\text{P}_2\text{O}_5+\text{Al}_2\text{O}_3} + W_{\text{Cu-SAPO-34-P}n} \times 85\%)$ . <sup>c</sup>Determined by XRF. <sup>d</sup>Calculation based on the following equation: Yield =  $W_{\text{synthesized materials}} \times 85\% / (W_{\text{SiO}_2+\text{P}_2\text{O}_5+\text{Al}_2\text{O}_3} + W_{\text{Cu-SAPO-34-P}n} \times 85\%)$ . <sup>e</sup>Synthetic details can be found in the supporting information.

amount of Cu-SAPO-34-*P<sub>n</sub>* precursor ranged from 17 wt%–60 wt%. The reactant gels were sealed in stainless-steel autoclaves and heated to 200 °C for 24 h with rotation. The samples were recovered by filtration, washed with distilled water, and dried at 120 °C in air overnight. Before the catalytic tests, the samples were calcined at 600 °C for 3 h to remove the templates. More details are listed in Table 1.

## 2.2. Characterization

Elemental analysis of the samples was carried out using a Philips Magix-601 XRF spectrometer. The powder XRD patterns were recorded on a PANalytical X'Pert PRO X-ray diffractometer with Cu-*K*<sub>α</sub> radiation ( $\lambda = 1.54059 \text{ \AA}$ ) generated at 40 kV and 40 mA. The textural properties of the calcined samples were determined by N<sub>2</sub> adsorption at -196 °C on a Micromeritics ASAP 2020 system. The total surface area was calculated using the Brunauer-Emmett-Teller (BET) equation, and the micropore volume and surface area were determined by using the *t*-plot method. DRIFT spectra were recorded on a Varian Cary-5000 UV-Vis-near infrared (NIR) spectrophotometer equipped with an integrating sphere, and the background of the UV-Vis spectrum was plotted against a BaSO<sub>4</sub> reference standard. The morphology of the samples was observed by SEM on a Hitachi SU8020 field-emission (FE) SEM device. EDX measurements conducted on the same Hitachi SU8020 FE-SEM device equipped with a Horiba X-Max silicon drift X-ray detector. The <sup>13</sup>C and <sup>29</sup>Si MAS NMR spectra were recorded on a Bruker Avance III 600 spectrometer equipped with a 14.1-T wide-bore magnet. The resonance frequencies were 100.5 and 119.2 MHz for <sup>13</sup>C and <sup>29</sup>Si, respectively. The spinning rates of the samples at the magic angle for <sup>13</sup>C and <sup>29</sup>Si were 8 and 6 kHz, respectively. The reference material for the chemical shift (in parts per million (ppm)) determination for <sup>13</sup>C and <sup>29</sup>Si was the sodium salt of 2,2-dimethyl-2-silapentane-5-sulfonate (DSS). TGA and DTA were performed on a TA SDTQ600 analyzer at a temperature programmed rate of 10 °C/min under an air flow of

100 mL/min. The organic contents of the as-made materials were determined by elemental analysis performed with an Elementar Vario EL elemental analyzer.

The NH<sub>3</sub>-TPD experiments were conducted in a Micromeritics Autochem II 2920 device. In these tests, 100 mg of calcined sample particles (40–60 mesh) were loaded into a U-shaped quartz tube and pretreated at 650 °C for 1 h in He flow (30 mL/min) to remove any impurities and, then, treated in a gas mixture of 2% NH<sub>3</sub> and 98% He flow (30 mL/min) at 120 °C to saturate the sample surface with adsorbed NH<sub>3</sub> (60 min). Subsequently, He (30 mL/min) was purged through the sample for 30 min to remove the weakly adsorbed NH<sub>3</sub> molecules. The measurement of the desorption of NH<sub>3</sub> was performed from 100 to 600 °C (10 °C/min) under He flow (30 mL/min).

DRIFT spectra were recorded with a Bruker Tensor 27 Fourier transform infrared (FTIR) spectrometer equipped with a gas cell. For this analysis, 15 mg of calcined sample was loaded into the sample cup of the high-temperature reaction chamber. For the ammonia-adsorbed in situ DRIFTS experiments, the pretreatment was conducted at 550 °C in N<sub>2</sub> flow (20 mL/min) for 1 h before cooling to 150 °C. NH<sub>3</sub> adsorption was conducted with a 24 mL/min flow rate containing 0.083% NH<sub>3</sub> with N<sub>2</sub> balance for 30 min, and then the DRIFTS spectra were obtained at different temperatures (150–500 °C) in a flow of pure N<sub>2</sub> flow (20 mL/min). The in situ DRIFTS spectra were also measured during reaction at 200 °C. The preadsorption of NH<sub>3</sub> was similar to that described above but was carried out at 200 °C. After that, the sample was swept with pure N<sub>2</sub> flow (20 mL/min) for 20 min, and then treated with 0.083% of NO and 6.1% of O<sub>2</sub> with N<sub>2</sub> balance for 0–30 min. The DRIFTS spectra were obtained during this process. The spectra were treated by subtracting the background spectra recorded after exposing the sample to 20 mL/min pure N<sub>2</sub> at 200 °C.

EPR measurements were performed on a Bruker A200 spectrometer. The samples were sealed in quartz tubes and pretreated at 120 °C in pure N<sub>2</sub> flow for 12 h. During spectral

collection, the microwave power was 2 mW, and the frequency was 9.52 GHz. The sweep width was 2000 G, and the sweep time was 84 s, modulated at 100 kHz with a 2 G amplitude. A time constant of 41 ms was used. The spectra were collected at 102 K. For the quantification of isolated Cu<sup>2+</sup> species, copper sulfate solution was used as a standard (at 102 K).

The temperature-programmed reduction of hydrogen (H<sub>2</sub>-TPR) was measured on a Micromeritics Autochem II 2920 device. In the TPR experiments, 100 mg of calcined sample particles (40–60 mesh) was pretreated in Ar flow (30 mL/min) at 500 °C for 1 h to remove impurities and, then, cooled to 100 °C in Ar flow (30 mL/min). The H<sub>2</sub>-TPR experiments were carried out at a heating rate of 10 °C/min from 100 to 900 °C under a 10% H<sub>2</sub> and 90% Ar flow (30 mL/min), and the consumption of H<sub>2</sub> was determined using a thermal conductivity detector (TCD).

### 2.3. Catalyst evaluation

The catalytic activity for the NH<sub>3</sub>-SCR was determined using 60 mg of the Cu-SAPO-34 catalyst (60–80 mesh) mixed with 240 mg of quartz beads (60–80 mesh) in a fixed-bed quartz reactor (0.95-cm diameter), and a K-type thermocouple was placed in the center of the catalyst bed to determine the temperature of the catalyst. The reactant gases were regulated before entering the reactor using mass flow controllers (Brookers). All gas lines were heated to 100 °C to prevent the condensation of the vapor. The concentrations of the simulated gases were as follows: 0.05% NO, 0.05% NH<sub>3</sub>, 6.1% O<sub>2</sub>, 6.4% H<sub>2</sub>O, and N<sub>2</sub> balance. The total flow rate was 320 mL/min, and the corresponding gas hourly space velocity (GHSV) was 300000 h<sup>-1</sup>. The concentrations of NO<sub>x</sub> (NO and NO<sub>2</sub>) and N<sub>2</sub>O in the inlet and outlet gases were continually analyzed by FTIR (Tensor 27, Bruker) in a 2-m gas cell. All catalysts were pretreated in the simulated gases at 550 °C for 2 h before the activity tests. Catalytic activity tests were carried out over the temperature range of 150 to 500 °C, and the activity results were recorded after holding at each temperature for 40 min. The NO<sub>x</sub> conversion was calculated using Eq. (1).

$$\text{NO}_x \text{ conversion} = \frac{[(\text{NO} + \text{NO}_2)_{\text{in}} - (\text{NO} + \text{NO}_2)_{\text{out}}]}{(\text{NO} + \text{NO}_2)_{\text{in}}} \times 100\% \quad (1)$$

The N<sub>2</sub> selectivity was calculated using Eq. (2).

$$\text{N}_2 \text{ selectivity} = \frac{[(\text{NO} + \text{NO}_2 + \text{N}_2\text{O})_{\text{in}} - (\text{N}_2\text{O})_{\text{out}}]}{[(\text{NO} + \text{NO}_2)_{\text{in}} - (\text{NO} + \text{NO}_2)_{\text{out}}]} \times 100\% \quad (2)$$

### 2.4. Kinetics measurements

NH<sub>3</sub>-SCR kinetic tests were performed in the same quartz tube reactor using 16.5 mg of the catalyst mechanically mixed with 300 mg of quartz sand. The total flow rate was 930 mL/min, corresponding to a GHSV of 3300000 h<sup>-1</sup>. The turnover frequencies (TOF) were calculated using eqn. (3).

$$\text{TOF} = (\text{NO}_x \text{ conversion}) \times F / (22.4 \times M) \text{ (s}^{-1}\text{)} \quad (3)$$

Here, *F* is the flow rate of NO<sub>x</sub>, and *M* is the number of moles of Cu in the powdered catalyst.

### 2.5. Steam treatment

After the standard NH<sub>3</sub>-SCR evaluation, the samples were further heated to 600 °C in dry air for *ca.* 15 min in the quartz reactor. Subsequently, gas flow containing 10% water balanced with N<sub>2</sub> was passed through the sample at 800 °C for 16 h to achieve high-temperature hydrothermal treatment. The total flow rate was 253 mL/min. Before any characterization or evaluation, the steam-treated samples were further heated to 600 °C in dry air and then kept in an oven at 120 °C.

## 3. Results and discussion

### 3.1. Synthesis and characterization

Cu-SAPO-34 samples with varied Si and Cu contents were synthesized by the reconstruction strategy. The crystallization conditions, product compositions, and solid yields are listed in Table 1. It was found that the Cu content could be adjusted by altering the dosage of the Cu-SAPO-34-*P<sub>n</sub>* precursor (samples 1–3). Cu-SAPO-34 with a very low Cu loading can be directly synthesized in high solid yield by introducing a small amount of Cu-SAPO-34-*P<sub>n</sub>*, as seen for sample 1, LSiCu<sub>1.6</sub> and HSiCu<sub>1.7</sub>, for which direct synthesis using the Cu-TEPA template is challenging. The Cu content increased as the amount of precursor increased (samples 1–3). This result indicates that the precursor acts as an effective copper source in the crystallization process. The Si contents of sample 4 and Cu-SAPO-34-P1 were similar when the dosage of *x*SiO<sub>2</sub> was 0.6. This result suggests that the newly crystallized SAPO-34 should have a Si content comparable to that of the precursor under these reaction conditions. When the amount of *x*SiO<sub>2</sub> was reduced or increased while the other conditions remained constant, the Si contents decreased or increased, respectively, as shown for samples 2, 4, and 5. It should be noted that the Si content of the product is affected by the composition of precursor significantly, as seen for sample 5 and HSiCu<sub>3.5</sub>. Although the dosage of *x*SiO<sub>2</sub> for HSiCu<sub>3.5</sub> is lower than that of sample 5, the Si content of HSiCu<sub>3.5</sub> is higher because of the usage of Cu-SAPO-34-P3 with higher Si contents than Cu-SAPO-34-P1. On the basis of these results from the reconstruction process, four Cu-SAPO-34 samples with comparable Cu and Si contents were synthesized (denoted LSiCu<sub>1.6</sub>, HSiCu<sub>1.7</sub>, LSiCu<sub>3.4</sub>, and HSiCu<sub>3.5</sub>) and used for further study. L and H refer to low and high product Si contents respectively, and the number following Cu is the percentage Cu content as determined by XRF analyses.

The XRD patterns of LSiCu<sub>3.4</sub> and HSiCu<sub>3.5</sub> are displayed in Fig. 1. All the peaks can be indexed to the typical CHA structure. There are no peaks at 35.3° and 38.5°, suggesting the absence of CuO species and the advantage of the current synthesis in achieving a uniform Cu distribution. N<sub>2</sub> adsorption measurements were conducted, and the isotherms are shown in Fig. 2. Both LSiCu<sub>3.4</sub> and HSiCu<sub>3.5</sub> show typical type-I isotherms and have microporous surface areas of 521 and 535 m<sup>2</sup>/g, respectively. The micropore volumes were 0.26 and 0.28 cm<sup>3</sup>/g (Table S1), confirming their good crystallinity.

UV-Vis spectroscopy was used to identify the copper species in the products, and the spectra are shown in Fig. 3. Both spectra contain strong bands at 270 nm, comparable to that of

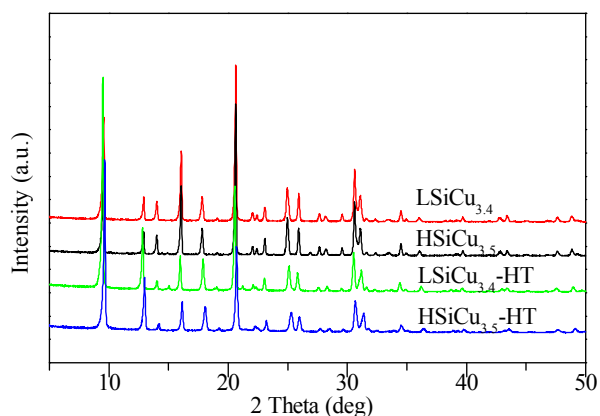


Fig. 1. XRD patterns of fresh and hydrothermally treated LSiCu<sub>3.4</sub> and HSiCu<sub>3.5</sub>.

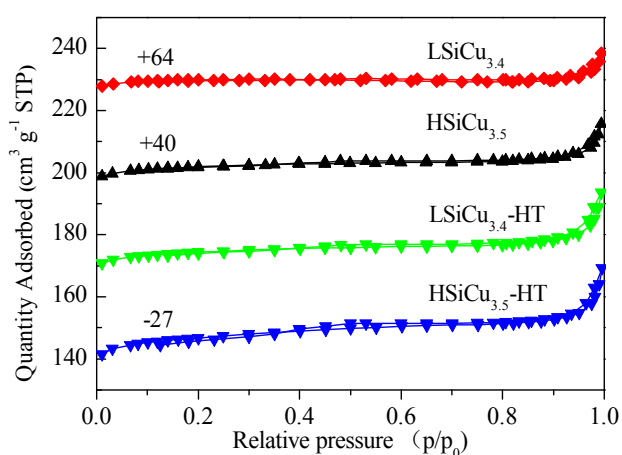


Fig. 2. N<sub>2</sub> adsorption-desorption isotherms of fresh and hydrothermally treated LSiCu<sub>3.4</sub> and HSiCu<sub>3.5</sub>.

Cu-SAPO-34-P2. This result indicates that the Cu species in the as-synthesized products were maintained, i.e., as the Cu-TEPA complex [19]. SEM and EDX analyses were performed to visualize the product morphology and Cu distribution, respectively, in the calcined products. Both LSiCu<sub>3.4</sub> and HSiCu<sub>3.5</sub> have typical

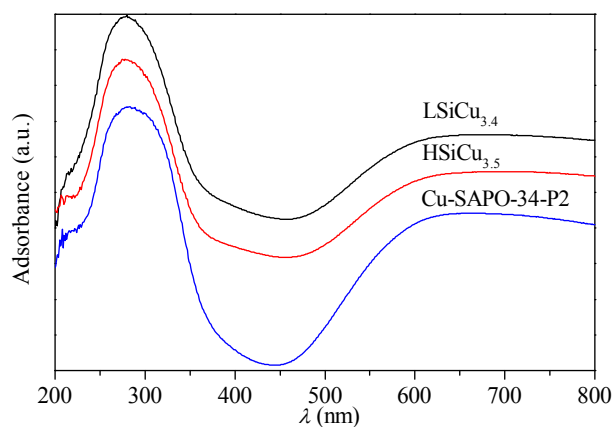


Fig. 3. UV-Vis spectra of as-synthesized LSiCu<sub>3.4</sub>, HSiCu<sub>3.5</sub>, and Cu-SAPO-34-P2.

rhombohedral morphologies with similar particle sizes of ca. 3–5 μm (Fig. 4). The EDX mapping images of Cu for LSiCu<sub>3.4</sub> and HSiCu<sub>3.4</sub> show highly dispersed light spots, as seen in the inset of Fig. 4. These results confirm that the precursor participates in the crystallization and the Cu species (Cu-TEPA complex) were incorporated into the Cu-SAPO-34 products uniformly.

Solid-state <sup>13</sup>C MAS NMR was employed to investigate the incorporated organic templates. The peak assignments are shown in Fig. 5. The peaks at 10 ppm are ascribed to the –CH<sub>3</sub> groups of DEA, and the peaks at around 41 ppm are obviously widened, probably arising from the combination of two signals from the –CH<sub>2</sub>– groups of DEA and those from the –CH<sub>2</sub>– groups linked to the primary amine groups of TEPA. The peaks at 48 ppm are assigned to –CH<sub>2</sub>– groups connected to the secondary amine groups of TEPA [23,24]. The results imply that both DEA and Cu-TEPA are still present in the samples. The exact molar ratio of TEPA/DEA was further estimated using TGA/DTA and elemental analyses. The results are listed in Table 2 and Fig. S4. Because the C/N ratio of DEA is 4 and that of TEPA is 1.6, the molar percent of TEPA in the full templates was calculated to be 21%; for comparison, 75 wt% content is obtained using the “one-pot” synthesis of Cu-SAPO-34 [21]. The obviously decreased Cu-TEPA content implies that the role of Cu-TEPA as a template was restricted by the CHA cage.

The chemical environments of the Si atoms in LSiCu<sub>3.4</sub> and

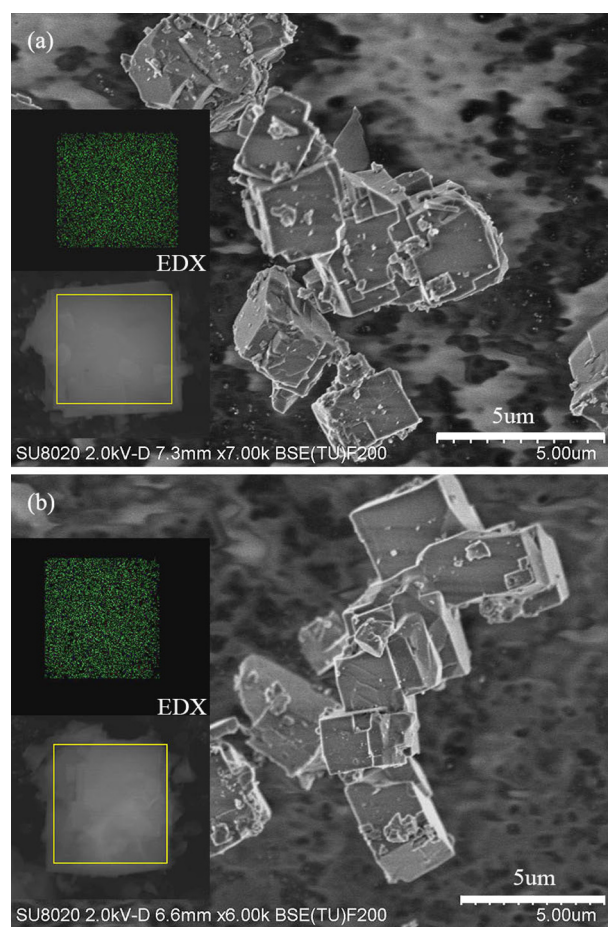


Fig. 4. SEM images and EDX mapping of Cu (Cu K<sub>α1</sub>) of calcined (a) LSiCu<sub>3.4</sub> and (b) HSiCu<sub>3.5</sub>.

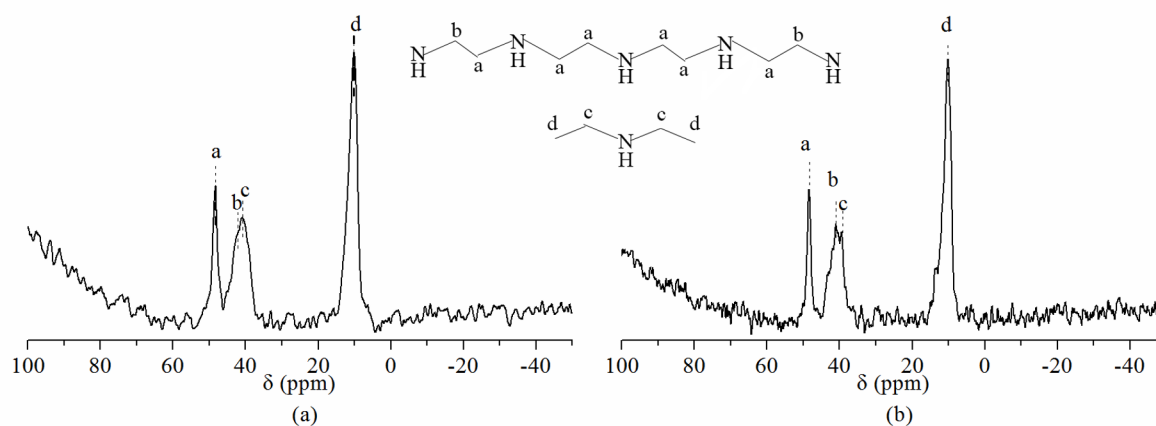


Fig. 5. Solid-state  $^{13}\text{C}$  MAS NMR spectra of as-synthesized (a)  $\text{LSiCu}_{3.4}$  and (b)  $\text{HSiCu}_{3.5}$ .

**Table 2**

Elemental analyses of as-synthesized  $\text{LSiCu}_{3.4}$  and  $\text{HSiCu}_{3.5}$ .

Sample	N (wt%)	C (wt%)	C/N ratio
$\text{LSiCu}_{3.4}$	3.7	8.3	2.7
$\text{HSiCu}_{3.5}$	3.9	8.9	2.6

$\text{HSiCu}_{3.5}$  were investigated using solid-state  $^{29}\text{Si}$  MAS NMR, and the spectra are shown in Fig. 6. In the spectrum of  $\text{LSiCu}_{3.5}$ , only a single signal at  $-91$  ppm was observed, and this is attributed to the  $\text{Si}(4\text{Al})$  species [25]. It is not surprised as the SAPO-34 directed by DEA template always has abundant  $\text{Si}(4\text{Al})$  environments [26]. The  $^{29}\text{Si}$  NMR spectrum of  $\text{HSiCu}_{3.4}$  is similar, but there is a small peak at  $-110$  ppm. The presence of this peak suggests that a very small number of Si islands were generated as the silica content increased. Nevertheless, the Si content and coordination environment have been better optimized compared to previous works [19,21]. The isolated  $\text{Si}(4\text{Al})$  coordination environment in the reconstructed Cu-SAPO-34 samples is beneficial for framework stability and the dispersion of  $\text{Cu}^{2+}$  ions [7,27]. A better  $\text{NH}_3$ -SCR activity is therefore expected which will be discussed in the following part.

### 3.2. $\text{NH}_3$ -SCR activity of the Cu-SAPO-34 catalysts

The  $\text{NH}_3$ -SCR activities of  $\text{LSiCu}_{3.4}$  and  $\text{HSiCu}_{3.5}$  were evaluated under standard  $\text{NH}_3$ -SCR conditions at a GHSV of  $300000 \text{ h}^{-1}$ . The reaction results are presented in Figs. 7a and S5. Both catalysts gave *ca.* 100%  $\text{N}_2$  selectivity over the whole reaction period. The  $\text{LSiCu}_{3.4}$  sample gave a high  $\text{NO}_x$  conversion of 51% at  $150^\circ\text{C}$ , which rapidly increased to 95% at  $175^\circ\text{C}$ , further increasing to 100% at  $200^\circ\text{C}$ . The  $\text{NO}_x$  conversion was maintained at 100% until  $350^\circ\text{C}$ . On further increasing the reaction temperature to  $400^\circ\text{C}$ , the conversion dropped to 94%, then decreasing to 89% at  $500^\circ\text{C}$ . Compared to  $\text{LSiCu}_{3.4}$ ,  $\text{HSiCu}_{3.5}$  shows an obviously lower  $\text{NO}_x$  conversion at low temperatures ( $150^\circ\text{C}$ , 40.8% and  $175^\circ\text{C}$ , 87.7%) but better performance at high temperatures ( $500^\circ\text{C}$ , 96%). The results suggest that, at an equal Cu loading level, the relatively low Si content of Cu-SAPO-34 may have a positive effect on the  $\text{NH}_3$ -SCR activity at low temperatures, whereas the high Si content benefits the activity at high temperature. This illustrates that the Si content (acidity) of the catalysts has a significant influence on the  $\text{NH}_3$ -SCR reaction. This hypothesis was further confirmed on the basis of the results obtained with  $\text{LSiCu}_{1.6}$  and  $\text{HSiCu}_{1.7}$ , whose catalytic performances show a similar trend (Fig. 7b). It is interesting to note that the activities of  $\text{LSiCu}_{1.6}$  and  $\text{HSiCu}_{3.5}$  are comparable, as shown in Fig. S6. These results demonstrate the importance of both Si and Cu species of Cu-SAPO-34 cata-

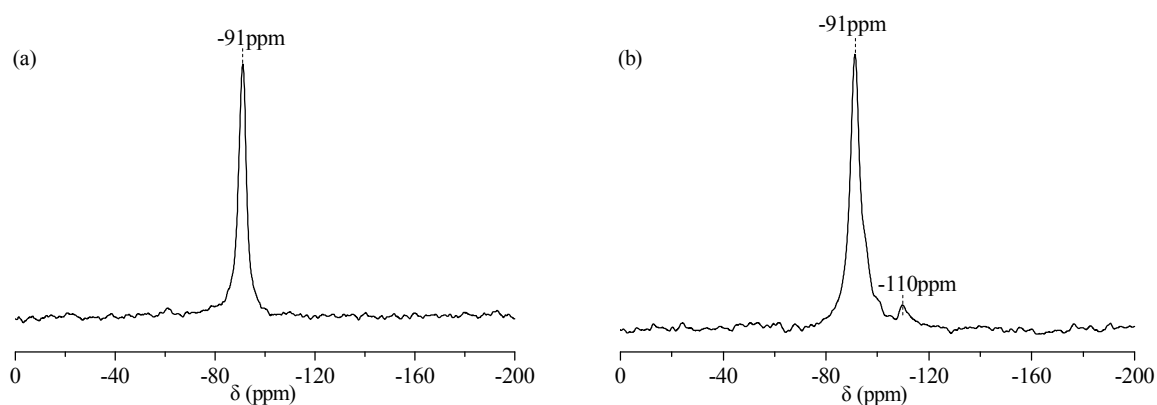
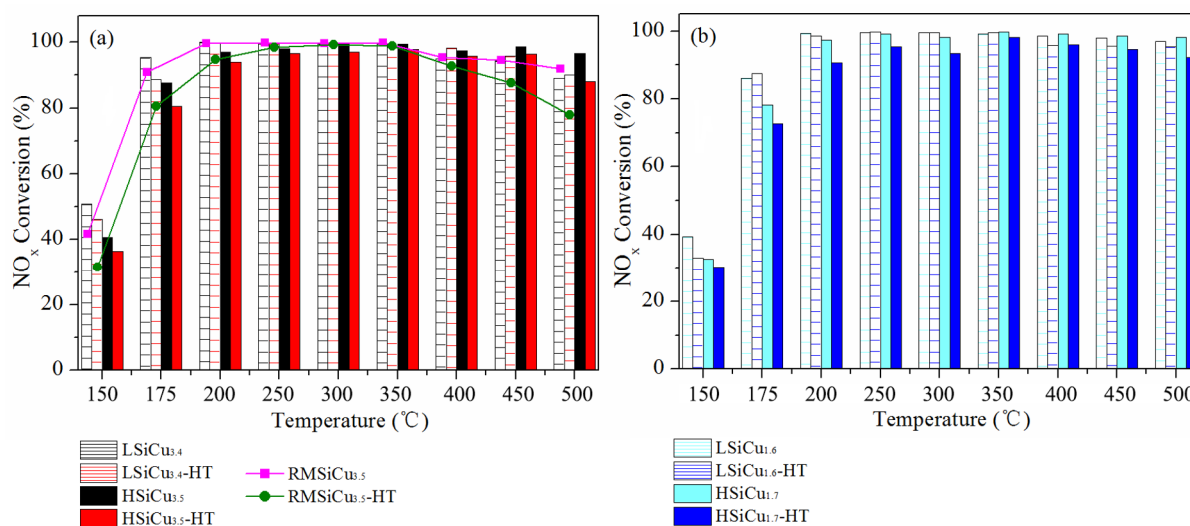


Fig. 6. Solid-state  $^{29}\text{Si}$  MAS NMR spectra of as-synthesized (a)  $\text{LSiCu}_{3.4}$  and (b)  $\text{HSiCu}_{3.5}$ .



**Fig. 7.** Standard  $\text{NH}_3$ -SCR reaction results over fresh and steam-treated (a)  $\text{LSiCu}_{3.4}$  and  $\text{HSiCu}_{3.5}$ , (b)  $\text{LSiCu}_{1.6}$  and  $\text{HSiCu}_{1.7}$ . The dotted lines in (a) indicate the results of using fresh (pink) and hydrothermally treated (green)  $\text{RMSiCu}_{3.5}$  as catalysts. The feed gas consisted of 0.05%  $\text{NH}_3$ , 0.05%  $\text{NO}$ , 6.1%  $\text{H}_2\text{O}$ , and 6.4%  $\text{H}_2\text{O}$  with  $\text{N}_2$  balance. GHSV = 300000  $\text{h}^{-1}$ . HT means high-temperature steam treatment (800 °C, 16 h).

lyst for the  $\text{NH}_3$ -SCR reaction.

Two kinds of reported Cu-SAPO-34 samples were used for comparison with our samples. The reported “one-pot” synthesized Cu-SAPO-34 (SAPO-34-7, 0.178 Si/ $\text{TO}_2$ , 3.1 wt% Cu) with Cu-TEPA as the Cu source and co-template showed an obviously lower  $\text{NO}_x$  conversion after hydrothermal treatment at 750 °C for 16 h, and the highest  $\text{NO}_x$  conversion decreased from ca. 95% to 70% [21]. The ion-exchanged Cu-SAPO-34 (0.167 Si/ $\text{TO}_2$ , 3.97 wt% Cu) [1] had lower catalyst activity, and its highest  $\text{NO}_x$  conversion was ca. 90% (GHSV = 240000  $\text{h}^{-1}$ ). However, the  $\text{NO}_x$  conversion was maintained well after steam treatment at 800 °C for 16 h. For comparison, we also prepared a “one-pot” Cu-SAPO-34 reference sample using Cu-TEPA and DEA as co-templates (denoted  $\text{RMSiCu}_{3.5}$ ). This sample had comparable Cu contents but medium Si contents. Although a 10 wt% nanosized SAPO-34 seed was used to induce the crystallization of  $\text{RMSiCu}_{3.5}$ , the crystallinity (Table S1) and solid yield (40.0 wt%) were still low. As shown in Fig. 7, the  $\text{NO}_x$  conversion of  $\text{RMSiCu}_{3.5}$  lies between those of  $\text{LSiCu}_{3.4}$  and  $\text{HSiCu}_{3.5}$ , but it shows more serious deterioration in activity upon hydrothermal treatment at 800 °C for 16 h. The loss in activity for  $\text{LSiCu}_{3.4}$  and  $\text{HSiCu}_{3.5}$  are less than 10%, whereas the loss in activity reached 24% for  $\text{RMSiCu}_{3.5}$  (Table 3). The results demonstrate the better hydrothermal stability of the reconstructed Cu-SAPO-34 and is comparable to that of ion-exchanged Cu-SAPO-34 [11].

Kinetic measurements were carried out to determine the

TOF and apparent activation energy ( $E_a$ ) and evaluate the reason for the activity difference between the reconstructed and “one-pot” synthesized samples in the  $\text{NH}_3$ -SCR reaction. For the kinetic tests, a GHSV of 3300000  $\text{h}^{-1}$  and pellet diameter of 60–80 mesh were employed to eliminate the influence of diffusion limitations [28]. Fig. 8 shows the Arrhenius plots of  $\text{LSiCu}_{3.4}$ ,  $\text{HSiCu}_{3.5}$ , and  $\text{RMSiCu}_{3.5}$ , and the plots were used to calculate the  $E_a$  values.  $\text{LSiCu}_{3.4}$  has the smallest  $E_a$  value of the three fresh samples, suggesting that it has the lowest activation barrier for the  $\text{NH}_3$ -SCR in the temperature range of 150–210 °C. After hydrothermal treatment, the TOF values of the samples decreased as the  $E_a$  values rose. The  $\text{RMSiCu}_{3.5}$ -HT sample presented the most significant increase in the  $E_a$  value, which is obviously higher than those of the other two samples, indicating the superior  $\text{NH}_3$ -SCR performance and hydrothermal stability of the reconstructed Cu-SAPO-34 samples.

### 3.3. Investigation of the catalyst acidity

The  $\text{NH}_3$ -TPD profiles of the samples are shown in Fig. 9. Each desorption curve can be decomposed into three peaks centered at ca. 190 °C (arising from weak acid sites from surface hydroxyl groups), 290 °C (arising from moderate acid sites, i.e., both Lewis acid sites related to Cu species and structural Brönsted acid sites), and 440 °C (assigned to strong Brönsted acid sites) [29]. The TPD profile of  $\text{HSiCu}_{3.5}$  contains a larger desorption peak area and higher  $\text{NH}_3$  desorption temperature

**Table 3**

Selected  $\text{NO}_x$  conversions of samples at 150, 200, and 500 °C.

Sample	Conversion of fresh samples (%)		Conversion of hydrothermally treated samples (%)		Reduction in conversion after steam treatment <sup>a</sup> (%)	
	150 °C	500 °C	150 °C	500 °C	150 °C	500 °C
$\text{LSiCu}_{3.4}$	51	89	46	90	9.8	-1
$\text{HSiCu}_{3.5}$	41	96	37	89	9.8	7.3
$\text{RMSiCu}_{3.5}$	41	92	31	78	24.4	15.2

<sup>a</sup> Loss in conversion =  $(\text{Conversion}_{\text{fresh}} - \text{Conversion}_{\text{HT}}) / \text{Conversion}_{\text{fresh}}$ .

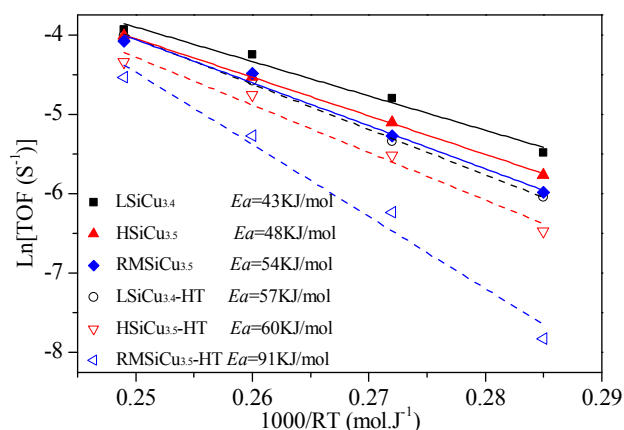


**Fig. 8.** Arrhenius plots of the Cu-SAPO-34 catalysts before and after hydrothermal treatment. The feed gas consisted of 0.05%  $\text{NH}_3$ , 0.05%  $\text{NO}$ , 6.1%  $\text{H}_2\text{O}$ , and 6.4%  $\text{H}_2\text{O}$  with  $\text{N}_2$  balance. GHSV = 3300000  $\text{h}^{-1}$ .

than those of  $\text{LSiCu}_{3.4}$ , suggesting that it has more acid sites and stronger acidity. The  $\text{NH}_3$ -TPD process was further investigated using in situ DRIFTS difference spectra. In Fig. 10, the negative band at  $3673 \text{ cm}^{-1}$  can be assigned to P-OH sites occupied by  $\text{NH}_3$ , and the bands at  $3621$  and  $3600 \text{ cm}^{-1}$  are caused by the depletion of Si-OH-Al acid sites by  $\text{NH}_3$  [30,31]. The bands at  $3271$  and  $1459 \text{ cm}^{-1}$  can be assigned to the stretching and bending vibrations of  $\text{NH}_4^+$  species adsorbed on Brönsted acid sites, and the bands at  $3184$  and  $1278 \text{ cm}^{-1}$  are attributed to  $\text{NH}_3$  adsorbed on Lewis acid sites. As the temperature was increased,  $\text{NH}_3$  desorption occurred, resulting in a decrease (or even disappearance) in the band intensity. The bands at  $3621$ ,  $3600$ ,  $3271$ , and  $1459 \text{ cm}^{-1}$  became very weak at  $400 \text{ }^\circ\text{C}$  for  $\text{LSiCu}_{3.4}$ , but they are still distinct in the spectrum of  $\text{HSiCu}_{3.5}$ . This result again indicates again that the Brönsted acid sites of  $\text{HSiCu}_{3.5}$  have stronger adsorption capacity than those of  $\text{LSiCu}_{3.4}$ .

Because a higher number of acid sites can better inhibit the  $\text{NH}_3$  oxidation reaction and improve the  $\text{NO}$  conversion at high temperatures [29,32], the observation of improved high-temperature  $\text{NH}_3$ -SCR catalytic performance on  $\text{HSiCu}_{3.5}$  is understandable. However, the reason for its inferior

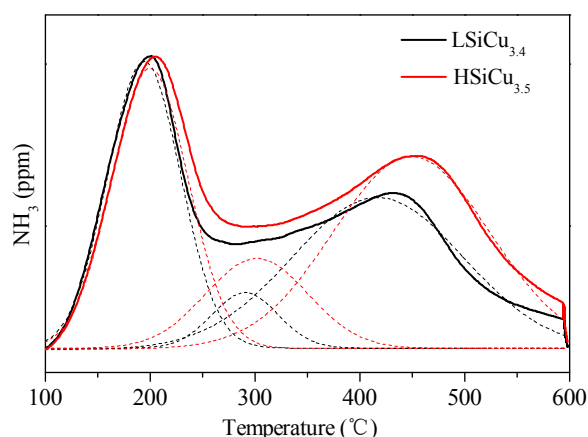


**Fig. 9.**  $\text{NH}_3$ -TPD profiles of  $\text{LSiCu}_{3.4}$  and  $\text{HSiCu}_{3.5}$ . The dotted lines represent the fitting results.

low-temperature  $\text{NH}_3$ -SCR activity merits investigation. Wang et al. [22] reported that a lower number of Brönsted acid sites results in fewer available  $\text{NH}_4^+$  species, thus resulting in lower  $\text{NH}_3$ -SCR activity. However, the acid strength was not considered in their research. Li et al. [33] found  $\text{NH}_3$  migration is slower than the  $\text{NH}_3$ -SCR reaction at low temperature range. Thus, the stronger Brönsted acidity of  $\text{HSiCu}_{3.5}$  may cause slower  $\text{NH}_3$  migration to the active Cu sites, which is disadvantageous for the  $\text{NH}_3$ -SCR reaction. To verify this speculation, samples with preadsorbed  $\text{NH}_3$  were exposed in  $\text{NO-O}_2$  gas at  $200 \text{ }^\circ\text{C}$  and monitored by in situ DRIFTS. As shown in Figs. 11a and 11b, all the peak intensities decrease with prolonged exposure time. The peak intensity at  $3271 \text{ cm}^{-1}$ , which represents the amount of  $\text{NH}_4^+$  at Brönsted acid sites [31], decreases slowly for  $\text{HSiCu}_{3.5}$  (Fig. 11c), verifying the lower activity of  $\text{NH}_3$  adsorbed on the Brönsted acid sites of  $\text{HSiCu}_{3.5}$ .

### 3.4. Cu species characterization

It is well accepted that Cu species play a crucial role in the  $\text{NH}_3$ -SCR reaction. EPR measurements were conducted because EPR can be used to quantify isolated  $\text{Cu}^{2+}$  ions while not detecting species such as  $\text{CuO}$ ,  $\text{Cu}^+$ , and  $[\text{Cu-O-Cu}]^{2+}$  [34]. The EPR

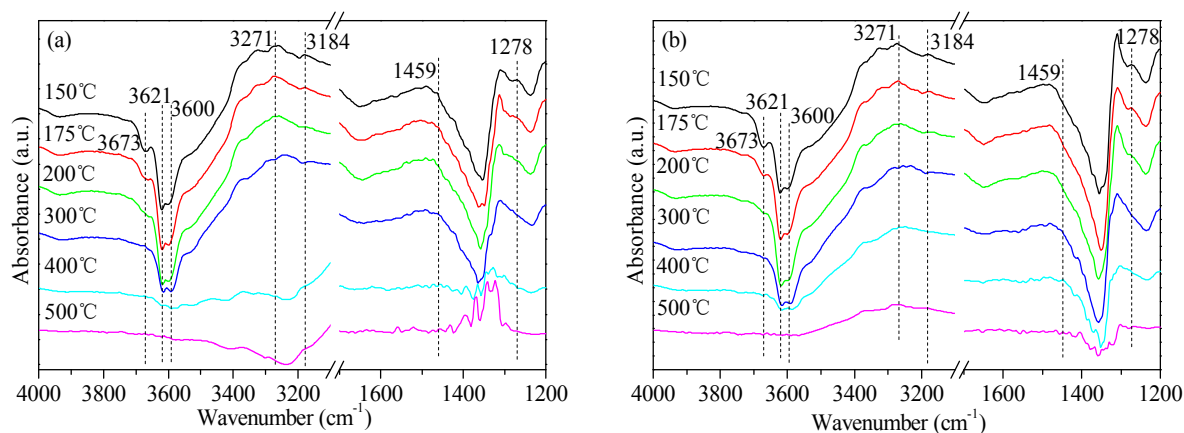


**Fig. 10.** In situ DRIFTS difference spectra of  $\text{NH}_3$  adsorbed on calcined (a)  $\text{LSiCu}_{3.4}$  and (b)  $\text{HSiCu}_{3.5}$  at various temperatures.

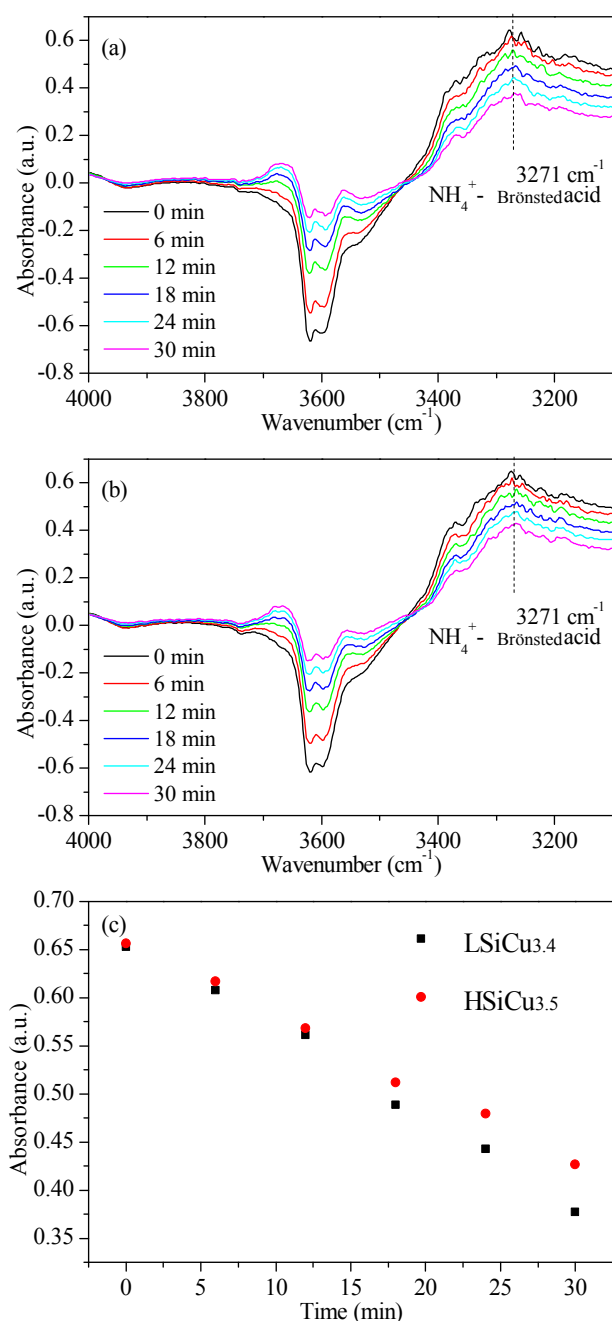


**Fig. 11.** In situ DRIFTS spectra of NH<sub>3</sub> adsorbed (a) LSiCu<sub>3.4</sub> and (b) HSiCu<sub>3.5</sub> exposed to NO-O<sub>2</sub> gas at 200 °C for different times. (c) The change in peak intensity at 3271 cm<sup>-1</sup> with exposure time.

spectra of LSiCu<sub>3.4</sub> and HSiCu<sub>3.5</sub> are similar, as shown in Fig. 12, and only one type of Cu species with signals of  $g_{\parallel} = 2.36$  and  $A_{\parallel} = 139$  G was identified. This result implies that all samples have only one type of isolated Cu<sup>2+</sup> species located at the double six-membered-rings (site I) [28,35] under the current measurement conditions, and steam treatment had a limited effect on the location of Cu<sup>2+</sup> ions. The isolated Cu<sup>2+</sup> ion contents were estimated from the EPR spectra, and the results are listed in Table 4. The calculated Cu contents are lower than those obtained from the XRF results because of the existence of other Cu species [34,36]. HSiCu<sub>3.5</sub> has more isolated Cu<sup>2+</sup> ions than

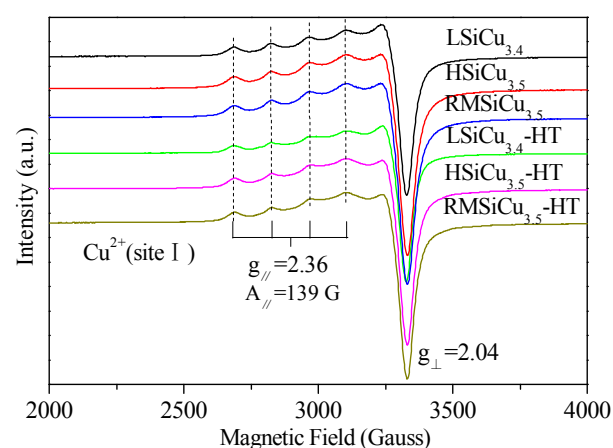


**Fig. 12.** EPR spectra of the fresh and hydrothermally treated LSiCu<sub>3.4</sub>, HSiCu<sub>3.5</sub>, and RMSiCu<sub>3.5</sub> samples.

LSiCu<sub>3.4</sub>. Given their similar Cu loadings, we can infer that the larger number of acid sites on HSiCu<sub>3.5</sub> is beneficial for stabilizing the isolated Cu<sup>2+</sup> ions. It has been recognized that a higher isolated Cu<sup>2+</sup> ion content is conducive to the NH<sub>3</sub>-SCR catalytic activity at low temperatures [36]. Therefore, the lower catalytic activity of HSiCu<sub>3.5</sub> at low temperatures compared to that of LSiCu<sub>3.4</sub> implies that the acidity of Cu-SAPO-34 plays a more important role than expected in the low-temperature NH<sub>3</sub>-SCR activity. The isolated Cu<sup>2+</sup> contents increase at a comparable level for the investigated samples after high-temperature steam treatment, indicating that the high-temperature treatment has a beneficial effect on the distribution of Cu<sup>2+</sup> ions.

H<sub>2</sub>-TPR was employed to probe the reducibility of the Cu species. The TPR profiles of the three samples present two main reduction peaks at ca. 240 and 600 °C, as seen in Fig. 13. The low-temperature peak is attributed to the reduction of isolated Cu<sup>2+</sup> to Cu<sup>+</sup>, and the high-temperature peak is due to the further reduction of Cu<sup>+</sup> to Cu<sup>0</sup> [37–40]. The small shoulder peaks at 175 °C for HSiCu<sub>3.5</sub> and RMSiCu<sub>3.5</sub> represents the reduction of nanosized CuO to Cu<sup>0</sup> [39]. After hydrothermal treatment, the high-temperature peaks moved to 700–800 °C, and their intensities decreased obviously, implying a more difficult reduction for Cu<sup>+</sup> ions. This is likely owing to the better redistribution of isolated Cu<sup>2+</sup> ions during aging. Moreover, a new peak at ca. 450 °C appeared for aged RMSiCu<sub>3.5</sub> (sample RMSiCu<sub>3.5</sub>-HT), suggesting the formation of bulk CuO species. Comparatively, the reconstructed samples have better resistance to steam treatment, showing little change in Cu species as compared to RMSiCu<sub>3.5</sub>. This is consistent with the better catalytic performance of the aged reconstructed samples.

**Table 4**

Isolated Cu<sup>2+</sup> ion content determined using EPR measurements in the fresh and hydrothermally treated LSiCu<sub>3.4</sub>, HSiCu<sub>3.5</sub>, and RMSiCu<sub>3.5</sub>.

Sample	Fresh (wt%)	Steam treated (wt%)
LSiCu <sub>3.4</sub>	1.67	1.93
HSiCu <sub>3.5</sub>	2.49	2.89
RMSiCu <sub>3.5</sub>	1.43	1.76

<sup>a</sup> 800 °C, 16 h.

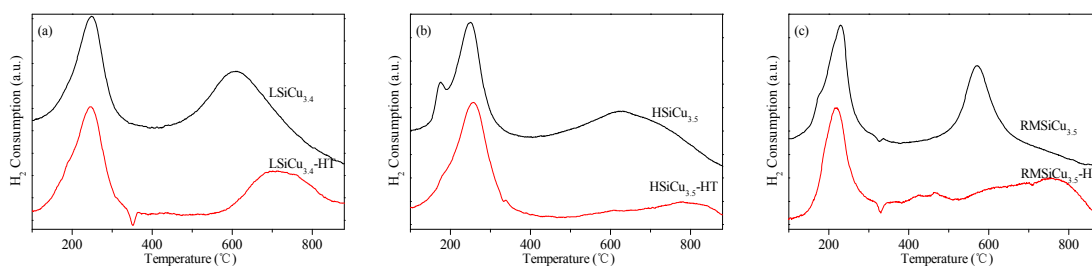


Fig. 13. H<sub>2</sub>-TPR profiles of the fresh and hydrothermally treated (a) LSiCu<sub>3.4</sub>, (b) HSiCu<sub>3.5</sub>, and (c) RMSiCu<sub>3.5</sub>.

#### 4. Conclusions

A new reconstruction strategy has been developed to synthesize Cu-SAPO-34 catalysts, which offers a wide crystallization phase region and allows an easy control over the Si and Cu contents. The resultant Cu-SAPO-34 has a dominant distribution of Si(4Al) coordination sites due to the restricted template role of Cu-TEPA in the precursor. Excellent NH<sub>3</sub>-SCR catalytic performance and enhanced resistance to hydrothermal conditions were achieved using the Cu-SAPO-34 catalyst prepared by the reconstruction method. Our investigation revealed that the acidity of Cu-SAPO-34 has a great effect on the NH<sub>3</sub>-SCR activity and hydrothermal stability. The weaker acidity is beneficial for low-temperature NH<sub>3</sub>-SCR activity. Therefore, the control of the Si content and distribution are crucial for catalyst optimization. These results suggest that Cu-SAPO-34 catalyst prepared by the reconstruction method is a promising candidate for the NH<sub>3</sub>-SCR process.

#### References

- [1] E. Borfecchia, P. Beato, S. Svelle, U. Olsbye, C. Lamberti, S. Bordiga, *Chem. Soc. Rev.*, **2018**, 47, 8097–8133.
- [2] P. Granger, V. I. Parvulescu, *Chem. Rev.*, **2011**, 111, 3155–3207.
- [3] S. C. Anenberg, J. Miller, R. M. Injares, L. Du, D. K. Henze, F. Lacey, C. S. Malley, L. Emberson, V. Franco, Z. Klimont, C. Heyes, *Nature*, **2017**, 545, 467–471.
- [4] Y. Xin, Q. Li, Z. Zhang, *ChemCatChem*, **2018**, 10, 29–41.
- [5] A. M. Beale, F. Gao, I. Lezcano-Gonzalez, C. H. F. Peden, J. Szanyi, *Chem. Soc. Rev.*, **2015**, 44, 7371–7405.
- [6] Y. J. Li, W. K. Hall, *J. Catal.*, **1991**, 129, 202–215.
- [7] J. Wang, H. Zhao, G. Haller, Y. Li, *Appl. Catal. B-Environ.*, **2017**, 202, 346–354.
- [8] I. Bull, W. M. Xue, P. Burk, R. S. Boorse, W. M. Jaglowski, G. S. Koermer, A. Moini, J. A. Patchett, J. C. Dettling, M. T. Caudle, US Patent 7601662, **2009**.
- [9] P. J. Andersen, J. E. Bailie, J. L. Casci, H. Y. Chen, J. M. Fedeyko, R. K. S. Foo, R. R. Rajaram, WO Patent, 132452, **2008**.
- [10] D. W. Fickel, E. D'Addio, J. A. Lauterbach, R. F. Lobo, *Appl. Catal. B-Environ.*, **2011**, 102, 441–448.
- [11] D. Wang, Y. Jangjiou, Y. Liu, M. K. Sharma, J. Luo, J. Li, K. Kamasamudram, W. S. Epling, *Appl. Catal. B-Environ.*, **2015**, 165, 438–445.
- [12] L. Ma, Y. Cheng, G. Cavataio, R. W. McCabe, L. Fu, J. Li, *Chem. Eng. J.*, **2013**, 225, 323–330.
- [13] F. Gao, E. D. Walter, N. M. Washton, J. Szanyi, C. H. F. Peden, *ACS Catal.*, **2013**, 3, 2083–2093.
- [14] J. Fan, P. Ning, Y. Wang, Z. Song, X. Liu, H. Wang, J. Wang, L. Wang, Q. Zhang, *Chem. Eng. J.*, **2019**, 369, 908–919.
- [15] Y. Cao, S. Zou, L. Lan, Z. Yang, H. Xu, T. Lin, M. Gong, Y. Chen, *J. Mol. Catal. A-Chem.*, **2015**, 398, 304–311.
- [16] X. Xiang, M. Yang, B. Gao, Y. Qiao, P. Tian, S. Xu, Z. Liu, *RSC Adv.*, **2016**, 6, 12544–12552.
- [17] F. Gao, E. D. Walter, N. M. Washton, J. Szanyi, C. H. F. Peden, *Appl. Catal. B-Environ.*, **2015**, 162, 501–514.
- [18] L. M. Ren, L. F. Zhu, C. G. Yang, Y. M. Chen, Q. Sun, H. Y. Zhang, C. J. Li, F. Nawaz, X. J. Meng, F. S. Xiao, *Chem. Commun.*, **2011**, 47, 9789–9791.
- [19] R. Martinez-Franco, M. Moliner, C. Franch, A. Kustov, A. Corma, *Appl. Catal. B-Environ.*, **2012**, 127, 273–280.
- [20] A. Turrina, E. C. V. Eschenroeder, B. E. Bode, J. E. Collier, D. C. Apperley, P. A. Cox, J. L. Casci, P. A. Wright, *Microporous Mesoporous Mater.*, **2015**, 215, 154–167.

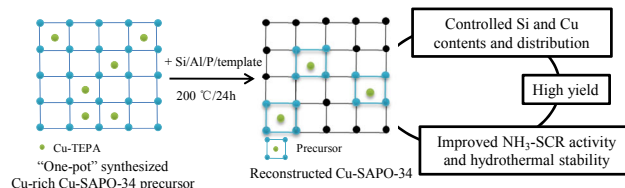
#### Graphical Abstract

*Chin. J. Catal.*, 2020, 41: 1410–1420 doi: 10.1016/S1872-2067(20)63583-5

#### A reconstruction strategy for the synthesis of Cu-SAPO-34 with excellent NH<sub>3</sub>-SCR catalytic performance and hydrothermal stability

Lijing Sun, Miao Yang, Yi Cao, Peng Tian\*, Pengfei Wu, Lei Cao, Shutao Xu, Shu Zeng, Zhongmin Liu\*  
*Dalian Institute of Chemical Physics, Chinese Academy of Sciences; University of Chinese Academy of Sciences; Ningbo University*

Cu-SAPO-34 was synthesized by employing Cu-rich SAPO-34 as a precursor and copper source. The template role of Cu-TEPA was limited during the recrystallization, which allowed the control of the Si and Cu contents and distribution in the products.



- [21] R. Martinez-Franco, M. Moliner, P. Concepcion, J. R. Thogersen, A. Corma, *J. Catal.*, **2014**, 314, 73–82.
- [22] L. Wang, W. Li, S. J. Schmiege, D. Weng, *J. Catal.*, **2015**, 324, 98–106.
- [23] D. Fan, P. Tian, S. Xu, Q. Xia, X. Su, L. Zhang, Y. Zhang, Y. He, Z. Liu, *J. Mater. Chem.*, **2012**, 22, 6568–6574.
- [24] C. Pellegrino, R. Aiello, F. Testa, F. Crea, A. Tuel, J. B. Nagy, *Microporous Mesoporous Mater.*, **2001**, 47, 85–96.
- [25] D. Wang, P. Tian, M. Yang, S. Xu, D. Fan, X. Su, Y. Yang, C. Wang, Z. Liu, *Microporous Mesoporous Mater.*, **2014**, 194, 8–14.
- [26] G. Liu, P. Tian, Z. Liu, *Chin. J. Catal.*, **2012**, 33, 174–182.
- [27] X. Xiang, P. Wu, Y. Cao, L. Cao, Q. Wang, S. Xu, P. Tian, Z. Liu, *Chin. J. Catal.*, **2017**, 38, 918–927.
- [28] Y. Cao, D. Fan, P. Tian, L. Cao, T. Sun, S. Xu, M. Yang, Z. Liu, *Chem. Eng. J.*, **2018**, 354, 85–92.
- [29] Z. Chen, C. Fan, L. Pang, S. Ming, W. Guo, P. Liu, H. Chen, T. Li, *Chem. Eng. J.*, **2018**, 348, 608–617.
- [30] L. Wang, W. Li, G. Qi, D. Weng, *J. Catal.*, **2012**, 289, 21–29.
- [31] D. Wang, L. Zhang, K. Kamasamudram, W. S. Epling, *ACS Catal.*, **2013**, 3, 871–881.
- [32] T. Yu, D. Fan, T. Hao, J. Wang, M. Shen, W. Li, *Chem. Eng. J.*, **2014**, 243, 159–168.
- [33] T. Yu, J. Wang, M. Q. Shen, W. Li, *Catal. Sci. Technol.*, **2013**, 3, 3234–3241.
- [34] J. Wang, D. Fan, T. Yu, J. Wang, T. Hao, X. Hu, M. Shen, W. Li, *J. Catal.*, **2015**, 322, 84–90.
- [35] J. Zhong, J. Han, Y. Wei, S. Xu, T. Sun, X. Guo, C. Song, Z. Liu, *Chin. J. Catal.*, **2018**, 39, 1821–1831.
- [36] S. K. Fan, J. J. Xue, T. Yu, D. Q. Fan, T. Hao, M. Q. Shen, W. Li, *Catal. Sci. Technol.*, **2013**, 3, 2357–2364.
- [37] Y. Wan, J. X. Ma, Z. Wang, W. Zhou, S. Kaliaguine, *J. Catal.*, **2004**, 227, 242–252.
- [38] L. Wang, J. R. Gaudet, W. Li, D. Weng, *J. Catal.*, **2013**, 306, 68–77.
- [39] X. L. Shan, N. J. Guan, X. Zeng, J. X. Chen, S. H. Xiang, *Chin. J. Catal.*, **2001**, 22, 237–241.

## 重构法合成Cu-SAPO-34及其NH<sub>3</sub>-SCR催化性能

孙丽婧<sup>a,b</sup>, 杨 淼<sup>a</sup>, 曹 毅<sup>a,c</sup>, 田 鹏<sup>a,\*</sup>, 吴鹏飞<sup>a,b</sup>, 曹 磊<sup>a</sup>, 徐舒涛<sup>a</sup>, 曾 姝<sup>a,b</sup>, 刘中民<sup>a,#</sup>

<sup>a</sup>中国科学院大连化学物理研究所, 洁净能源国家实验室(筹), 甲醇制烯烃国家工程实验室, 辽宁大连116023

<sup>b</sup>中国科学院大学, 北京100049

<sup>c</sup>宁波大学材料科学与化学工程学院, 浙江宁波315211

**摘要:** 氨选择催化还原NO<sub>x</sub>(NH<sub>3</sub>-SCR)是重要的柴油车尾气脱硝技术。发展高效且稳定的催化剂是提升该技术指标、应对严苛排放标准的关键。近年来,以Cu-SSZ-13和Cu-SAPO-34为代表的金属离子负载分子筛催化剂材料因其较宽的活性温度窗口和高水热稳定性受到研究者的广泛关注。Cu-SSZ-13分子筛催化剂已被BASF公司商业应用。相较Cu-SSZ-13, Cu-SAPO-34具有更优的低温活性与高温水热稳定性,且合成成本低廉。但Cu-SAPO-34的低温耐水性差,当采用传统的金属离子负载过程进行反复多次离子交换时,存在分子筛结晶度下降(部分骨架结构塌陷)的风险。使用铜四乙烯五胺络合物(Cu-TEPA)作为模板剂和铜源一步合成Cu-SAPO-34可以避免反复的离子交换过程,但由于Cu-TEPA的模板导向能力过强, Cu负载量难以控制,而降低Cu-TEPA的投料量则会损失产品收率。同时,该方法合成的Cu-SAPO-34中含有大量硅岛,分子筛催化剂的水热稳定性显著降低。针对这些问题,本文提出利用一步合成的高铜含量Cu-SAPO-34作为前驱体与铜源合成Cu-SAPO-34的方法(命名为重构法)。该方法不仅产品收率高,而且Cu和Si的含量/分布可控,合成样品的NH<sub>3</sub>-SCR催化性能和水热稳定性也明显提升。

EDX结果显示,焙烧后的Cu-SAPO-34中铜分布均匀,说明前驱体充分参与了Cu-SAPO-34的重构。<sup>13</sup>C NMR和元素分析结果显示,相较一步法合成的Cu-SAPO-34,重构的Cu-SAPO-34中的四乙烯五胺在模板剂中的比例明显下降。Cu-TEPA限域在前驱体的CHA笼中,有效抑制其结构导向剂的作用。Cu引入量由前驱体加入量决定。<sup>29</sup>Si NMR结果显示, Cu-SAPO-34中的硅主要呈Si(4Al)分布,这有利于Cu-SAPO-34保持良好的高温水热稳定性。NH<sub>3</sub>-SCR反应结果显示,相较一步法合成的Cu-SAPO-34,重构的Cu-SAPO-34表现出良好的NH<sub>3</sub>-SCR反应活性和更优异的高温水热稳定性。不同硅含量的重构Cu-SAPO-34的NH<sub>3</sub>-SCR反应结果显示:在低温段,低硅含量的Cu-SAPO-34具有更高的反应活性;在高温段,高硅含量的Cu-SAPO-34具有更高的反应活性。通过NH<sub>3</sub>-TPD和原位红外漫反射分析发现,低硅含量的Cu-SAPO-34具有相对较弱的酸性,使得吸附的氨具有较高的反应性,催化剂的低温活性较高。

**关键词:** Cu-SAPO-34; 水热合成; NH<sub>3</sub>-SCR; 水热稳定性; 晶化

收稿日期: 2020-01-16. 接受日期: 2020-02-27. 出版日期: 2020-09-05.

\*通讯联系人. 电话: (0411)84379218; 传真: (0411)84699289; 电子信箱: tianpeng@dicp.ac.cn

#通讯联系人. 电话: (0411)84379998; 传真: (0411)84379289; 电子信箱: liuzm@dicp.ac.cn

基金来源: 国家自然科学基金(21476228, 21606221, 21676262, 21991091), 中国科学院前沿科学重点研究计划(QYZDB-SSW-JSC0 40).

本文的电子版全文由Elsevier出版社在ScienceDirect上出版(<http://www.sciencedirect.com/science/journal/18722067>).